







Cite this: *New J. Chem.*, 2023, 47, 4577

Unprecedented Ir(III) cationic complexes based on tridentate tetrazolate ligands: synthesis, photophysics and encapsulation in SiO₂ nanoparticles†

José Troya,  ‡ María Mar Quesada-Moreno,  * Juan-Ramón Jiménez  and Juan Manuel Herrera  *

The first examples of luminescence Ir(III) complexes derived from a tridentate tetrazole ligand, 2-(tetrazole-5-yl)-1,10-phenanthroline (Hphenttz), are reported here. Two cationic complexes, heteroleptic [Ir(tpy)(phenttz)]²⁺ (**1**) (tpy = 2,2':6',2''-terpyridine) and homoleptic [Ir(phenttz)₂]³⁺ (**2**), have been synthesized and fully characterized from a chemical, structural and photophysical point of view. Both complexes exhibit green luminescence with a prevalent ³LC (Ligand-Centered) character, which is evidenced by their structured emission profiles and low *k_r* values (of about 10³ s⁻¹), and supported by density functional theory (DFT) and time-dependent density functional theory (TD-DFT) calculations. In air-equilibrated solutions, **1** and **2** show emission lifetimes (respective values of 1.6 μs and 1.2 μs) comparable to that of the reference complex [Ir(tpy)₂]³⁺ (1.0 μs) and quantum yields slightly lower (1.5% (**1**), 1.3% (**2**)) than that obtained for [Ir(tpy)₂]³⁺ (2.5%). Under an oxygen-free atmosphere, the emission lifetimes and quantum yields (τ/Φ) of the complexes increase significantly up to 5 μs/4.2% (**1**) and 3 μs/3.3% (**2**). **1** has been embedded within amorphous silica nanoparticles leading to the hybrid material **1**@SiO₂. This material shows enhanced photochemical stability and higher luminescence efficiency compared to the free complex, which demonstrates that silica hampers the diffusion of O₂, restrains the mobility of the complex and stimulates the radiative decay of the excited state.

Received 9th December 2022,
Accepted 23rd January 2023

DOI: 10.1039/d2nj06037j

rsc.li/njc

Introduction

Tetrazole compounds have attracted a lot of attention in the last few decades. In pharmacy, tetrazoles can replace the carboxyl group, enhance the lipophilicity and biocompatibility of drugs and reduce side effects. They have shown biological

activity as antitubercular, antimalarial or anticancer agents, and have been used in clinics for the treatment of various diseases.^{1,2} In the field of coordination chemistry, these ligands have also gathered much attention due to their ability to coordinate metal ions with a wide diversity of coordination modes.³ Their relatively easy synthesis has enabled the preparation of a plethora of 5-substituted tetrazole derivatives that can act as mono-, bi- or multi-dentate ligands.^{4–6} A vast number of robust coordination compounds with interesting structural, luminescence, zeolitic and magnetic properties have been studied in recent decades.^{7–14} In the photochemistry field, 5-substituted aryl-, pyridyl- or pyrazine- tetrazolates have been used profusely as ligands to prepare luminescence complexes based on lanthanides,^{15–22} Ru(II),^{23,24} Re(I),^{25–27} Pt(II),^{28–36} and Ir(III) metal ions, which are particularly interesting in this work. The 2-pyridyltetrazolate (pytz) anion was first used as an ancillary ligand to prepare a set of heteroleptic [Ir(C[^]N)(pytz)] neutral complexes used as dopants of blue-emitting OLEDs.^{37,38} Since then, the interest in the design of tetrazole-based luminescence Ir(III) complexes has grown considerably thanks to the easy functionalization of the ligand structure, which allows tuning of the color emission. Bidentate tetrazolate

Departamento de Química Inorgánica, Facultad de Ciencias, Unidad de Excelencia en Química Aplicada a Biomedicina y Medioambiente (UEQ), Universidad de Granada, Avda. Fuentenueva s/n, 18071, Granada, Spain.

E-mail: mqmoreno@ugr.es, jmherreira@ugr.es

† Electronic supplementary information (ESI) available: NMR (¹H, ¹³C and HH-2D-COSY) spectra of ligand Hphenttz and complexes **1** and **2**. Crystallographic data and selected bond distances and angles (experimental and TD-DFT calculated ones) for complexes **1** and **2**. Computed electronic transitions and calculated wavelengths and orbital transition analyses of the lowest energy emission band of complexes **1** and **2**. Experimental and fitting decay of the excited state in **1**, **1**@SiO₂ and **2**. Localization of the HOMO ±/LUMO± (1–3) for the ground and excited states of **1** and **2**. Additional TEM-images of **1**@SiO₂. Cyclic voltammograms of complexes **1** and **2**. CCDC 2221011 and 2221012. For ESI and crystallographic data in CIF or other electronic format see DOI: <https://doi.org/10.1039/d2nj06037j>

‡ Present address: Instituto de Ciencia Molecular (ICMol), Universidad de Valencia, Catedrático José Beltrán 2, 46980, Paterna, Spain.



ligands have been used as either cyclometallating or ancillary moieties to prepare neutral Ir(III) complexes whose color emission varied from blue to red. The reactivity of the tetrazolate rings towards electrophilic agents such as H^+ or CH_3^+ also contributed to tune their photoluminescent properties and modify their ionic nature; from neutral emitters used in the fabrication of OLEDs to cationic complexes used as dopants for LEECs devices. Additionally, they have been used as luminescent solar concentrators or anionic species to prepare multicolour-emitting soft salts when combined with luminescent counterions.^{39–42}

To date, all the luminescent Ir(III)-tetrazolate complexes reported in the literature have been prepared exclusively from mono- or bidentate ligands. Even though the synthesis of Ir(III) phosphors based on tridentate azolate chelates has demonstrated that a higher denticity implies a superior chemical stability of the complex towards metal-chelate dissociation,^{43–47} the use of tridentate tetrazolate ligands has been ignored. In this work, we report on the synthesis, structure and photophysical properties of two cationic Ir(III) complexes derived from the tridentate 2-(tetrazol-5-yl)-1,10-phenanthroline (Hphenttz) ligand: the heteroleptic complex $[Ir(tpy)(phenttz)]^{2+}$ (**1**) (tpy = 2,2':6',2''-terpyridine) and the homoleptic derivate $[Ir(phenttz)_2]^+$ (**2**) (Scheme 1). Additionally, **1** has been embedded within silica nanoparticles leading to the hybrid material **1@SiO₂**, whose photophysical properties have been compared with those of the free complex.

Experimental section

General procedures

The ligand 2,2':6',2''-terpyridine (tpy), $IrCl_3 \cdot xH_2O$, other reagents and common solvents were obtained from commercial sources and used as received. The ligand Hphenttz and Ir(III) precursor $[Ir(tpy)Cl_3]$ were synthesized following classical procedures described previously.^{14,48} The Ir(III) complexes **1** and **2** were

prepared in the dark under an Ar(g) inert atmosphere. Both complexes were purified by column chromatography using activated alumina (Brokmann, grade III) as the stationary phase and a mixture of CH_3CN/H_2O /saturated KNO_3 solution as the eluent, with proportions in volume ranging from 100/0/0 to 70/28/2. Single crystals were obtained by slow diffusion of Et_2O vapours into CH_3CN solutions of the respective complexes.

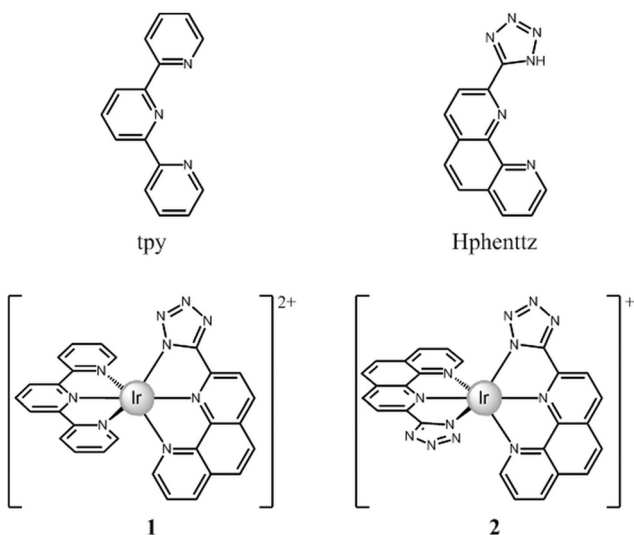
Syntheses

$[Ir(tpy)(phenttz)](PF_6)_2$ (1**).** $[Ir(tpy)Cl_3]$ (125 mg, 0.235 mmol), phenttz-H (65 mg, 0.260 mmol) and CH_3COONa (21 mg, 0.260 mmol) were mixed in 15 mL of degassed ethylene glycol and refluxed for 5 h. The resulting solution was cooled down and added to a water solution containing an excess of KPF_6 , which afforded an orange-brown precipitate that was purified by column chromatography. The final orange fraction was evaporated to dryness, dissolved in water and added to an aqueous solution of KPF_6 leading to the desired complex **1** as a red-brown solid (Yield: 34%). 1H NMR (400 MHz, $DMSO-d_6$, δ): 9.39 (d, $J = 8.7$ Hz, 1H), 9.24 (d, $J = 8.3$ Hz, 2H), 9.12 (d, $J = 8.7$ Hz, 1H), 8.94 (d, $J = 8.0$ Hz, 2H), 8.89 (dd, $J = 11.7, 8.3$ Hz, 2H), 8.67 (d, $J = 8.9$ Hz, 1H), 8.49 (d, $J = 9.0$ Hz, 1H), 8.41 (d, $J = 5.2$ Hz, 1H), 8.27 (td, $J = 7.9, 1.4$ Hz, 2H), 7.85 (dd, $J = 8.3, 5.3$ Hz, 1H), 7.63 (dd, $J = 5.7, 1.4$ Hz, 2H), 7.41 (ddd, $J = 7.4, 5.7, 1.4$ Hz, 2H). ^{13}C NMR (400 MHz, $DMSO-d_6$, δ): 154.91, 153.37, 143.08, 142.36, 140.72, 129.60, 129.45, 128.06, 127.37, 126.67, 125.77, 122.72. TOF-MS-ES+ (m/z): 816.09 ($M-PF_6^+$). Anal. calc. for $C_{28}H_{18}F_{12}IrN_9P_2 \cdot H_2O$: C, 34.29; N, 12.85; H, 2.06. Found: C, 34.60; N, 12.69; H, 2.26.

The complex was isolated as a nitrate salt by ion-exchange chromatography on a strong base anion exchanger type-III in its nitrate form, and using water as the eluent. The aqueous solution containing the complex was evaporated to dryness, dissolved in a minimum water quantity and precipitated with acetone.

$[Ir(phenttz)_2]PF_6$ (2**).** $IrCl_3$ (403 mg, 1.28 mmol) was mixed with a slight excess of the ligand phenttz-H (2.2 molar equiv.) and CH_3COONa (2.2 molar equiv.) in 15 mL of ethylene glycol and refluxed under an inert atmosphere for 6 hours. After this time, the mixture was cooled to room temperature and added to an excess of KPF_6 dissolved in water, which afforded a brownish yellow product that was purified by column chromatography. The yellow fraction containing the desired complex was evaporated to dryness, redissolved in water and added to an aqueous solution of KPF_6 (excess) leading to precipitation of **2** as a pale yellow solid (Yield: 72%). 1H NMR (400 MHz, ppm, $DMSO-d_6$, δ): 9.36 (d, 1H), 9.10 (d, 1H), 8.83 (d, 1H), 8.64 (d, 1H), 8.47 (d, 1H), 8.32 (d, 1H), 7.74 (dd, 1H). ^{13}C RMN (400 MHz, ppm, $DMSO-d_6$, δ): 164.63, 155.40, 149.13, 147.03, 146.20, 142.41, 140.81, 132.21, 130.10, 129.75, 128.20, 127.65, 122.15. TOF-MS-ES+ (m/z): 687.10 (M^+). Anal. calc. for $C_{26}H_{14}F_6IrN_{12}P \cdot CH_3CN \cdot H_2O$: C, 37.76; N, 20.44; H, 2.15. Found: C, 37.75; N, 20.26; H, 2.25.

Synthesis of **1@SiO₂ nanoparticles.** 1 mL of an aqueous solution of **1** in its nitrate form (15 mM) and 200 μ L of tetraethyl orthosilicate (TEOS) were added to a mixture of Triton X-100 (1.8 mL), hexanol (1.8 mL) and cyclohexane (7.5 mL) that was



Scheme 1 Tridentate ligands and cationic Ir(III) complexes studied in this work.



stirred until a clear microemulsion was formed. Then, 60 μL of concentrated NH_4OH were added to it and the mixture was stirred vigorously for 24 h. After this time, acetone was added to break the microemulsion and the nanoparticles were recovered by centrifugation, washed repeatedly with water, then with ethanol, and dried at 50 $^\circ\text{C}$ for 16 h.

X-ray crystallography

Suitable crystals of **1** and **2** were mounted on a Bruker D8 Venture diffractometer. Details of the crystals, data collection and refinement parameters are given in the ESI† (Table S1). After data processing (raw data integration, merging of equivalent reflections and absorption correction), the structures were solved by direct methods and refined using least squares minimization with the SHELX suite of programs⁴⁹ integrated in OLEX2.⁵⁰ Selected bonds and lengths are given in Tables S2 and S3 (ESI†). CCDC numbers 2221011 (**1**) and 2221012 (**2**) contain the supplementary crystallographic data for this article. These data are provided free of charge by the Cambridge Crystallographic Data Centre.

Physical measurements

Elemental analyses were carried out on a Fisons-Carlo Erba analyser model EA1108. NMR characterizations were performed on a 400 MHz (2 channels) BRUKER Nanobay Advance III. Emission and excitation spectra were measured using a UV-VIS-PTI QuantaMaster™ 8000 spectrofluorometer equipped with a Picosecond Photon Detector (230–850 nm, PPD-850, HORIBA Scientific) and a continuous Xenon Short Arc Lamp (190–2000 nm, USHIO). All the spectra (emission and excitation) were corrected with Real-time corrections function. TCSPC lifetime measurements were performed using a 375 nm excitation wavelength provided by a pulsed diode light source NanoLED 375L (<200ps pulse, HORIBA Scientific). Nanoparticles were characterized by transmission electron microscopy (TEM) using a LIBRA 120 PLUS Carl Zeiss electron microscope operating at 200 keV. 5 mg of the material was redispersed by sonication (30 min) in 1 mL of EtOH. Carbon reinforced copper grids (200 mesh) were submerged into suspension 50 times and then allowed to dry in air for at least 48 h. The size of the particles was determined by “manual counting” using ScionImage software (<https://www.scioncorp.com>). HAADF-STEM images and EDX analyses were recorded on a HAADF FEI TITAN G2 instrument working at an accelerating voltage of 200 kV in the scanning mode with a probe diameter of 0.5 nm.

All these techniques are available at the Centro de Instrumentación Científica (CIC) of the University of Granada.

Computational methodology

DFT (Density Functional Theory) calculations were performed using the long-range corrected CAM-B3LYP⁵¹ and the hybrid B3LYP^{52–54} functionals together with the 6-31G** basis set for

C, H, and N, and the “double- ζ ” quality LANL2DZ basis set for Ir.^{55–57} An effective core potential (ECP) replaces the inner core electrons of iridium, leaving the outer core $(5s)^2(5p)^6$ electrons and the $(5d)^6$ valence electrons of Ir(III). Implicit solvent (acetonitrile) effects were taken into account using the IEF-PCM formalism.⁵⁸ Time-dependent DFT (TD-DFT) calculations of the lowest-lying 10 singlets and 10 triplets were performed in the presence of the solvent at the minimum-energy geometry optimized for the ground states at CAM-B3LYP and B3LYP. The lowest energy triplet (T_1) excited states were optimized and tested to be real minima by carrying out vibrational frequency calculations (no imaginary frequency was found). Mulliken population analysis (MPA) was applied following the methodology used by Chi *et al.*⁴⁷ to obtain the electron density distribution of each atom in specific molecular orbitals of the Ir(III) compounds and to calculate the metal-to-ligand charge transfer (MLCT) character in each assignment of the singlet and triplet optical transitions. All the calculations were performed using the B.01 revision of the Gaussian 09 program package⁵⁹ and visualization of the orbitals was carried out by Avogadro.⁶⁰

Results and discussion

Synthesis and structural characterization

Heteroleptic complex **1** was prepared by reaction of the neutral precursor $[\text{Ir}(\text{tpy})\text{Cl}_3]$ with a slight excess of the deprotonated tetrazolate ligand phenttz in ethylene glycol at 180 $^\circ\text{C}$. The complex was purified by column chromatography and isolated as the hexafluorophosphate salt by anion exchange with KPF_6 . The addition of NaOAc helps to deprotonate the tetrazol ligand and improve the yield of the reaction.⁴⁴

Single crystals were obtained by slow diffusion of Et_2O in CH_3CN solutions of the complexes (Fig. 1). **1** crystallizes in the monoclinic $P2_1/c$ space group. The asymmetric unit shows one cationic $[\text{Ir}(\text{tpy})(\text{phenttz})]^{2+}$ (**1**) unit, the corresponding hexafluorophosphate counter-ions and an acetonitrile solvent molecule. Within the mononuclear unit, the Ir(III) centre exhibits a slightly distorted octahedral geometry. Tpy and the tetrazolate phenttz ligands act, as expected, as tridentate quelates adopting an orthogonal disposition (*mer*- isomers). The terpyridine chelate shows Ir– N_{tpy} bond distances between 1.972 and 2.060 Å, bite angles ($\text{N1}–\text{Ir}–\text{N2}$ and $\text{N2}–\text{Ir}–\text{N3}$) close to 80° and a *trans* $\text{N1}–\text{Ir}–\text{N3}$

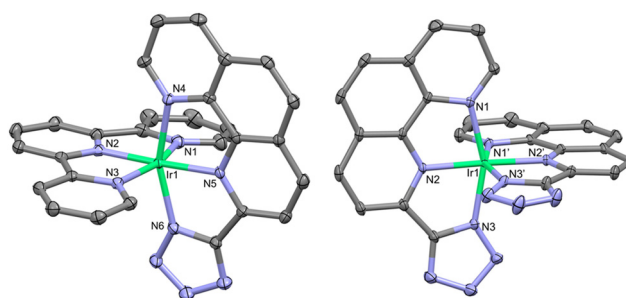


Fig. 1 X-Ray structures of complexes **1** (left) and **2** (right). ORTEP ellipsoids are at 50% probability. H atoms have been omitted for the sake of clarity.



angle of 159.63° (Table S2, ESI†). These values are almost identical to those reported for the homoleptic complex $[\text{Ir}(\text{tpy})_2](\text{PF}_6)_3$.⁶¹ With respect to the anionic tetrazolate moiety, the Ir–N_{tetrazolate} bond distance (2.047 (2) Å) is noticeably shorter than those found for Ir(III) complexes based on bidentate 2-pyridyl- and 2-pyrazine-tetrazolate ligands (2.137(15) Å – 2.147(3)).^{37,39} Intermolecular π – π interactions compatible with “terpyridine embrace” are detected between neighbouring mononuclear units, with interplanar distances of about 3.8 Å (Fig. S1, ESI†).

Complex **2** was prepared by reaction of IrCl_3 with 2.2 molar equivalents of Hphenttz in hot ethylene glycol in the presence of sodium acetate. The complex crystallizes in the monoclinic space group $C2/c$ and the asymmetric unit contains half of the metallic unit, with the other half generated by rotation about the C_2 axis that runs parallel to the b axis of the unit cell. The asymmetric unit also contains one hexafluorophosphate counter-ion with half occupancy and two solvated acetonitrile molecules. Bond distances and angles between the Ir(III) centre and the N atoms of the phenttz chelate are similar to those observed in **1** (Table S3, ESI†). Within the unit cell, intermolecular π – π stacking interactions are observed between the central rings of the phenanthroline units with an inter-centroid distance of 3.58 Å (Fig. S1, ESI†).

In both complexes, a notable pincer effect imposed by the five membered tetrazolate rings is observed, with bite and trans- angles less than 90° and 180° , respectively. This is the main factor accounting for the distorted octahedral coordination sphere around the Ir(III) centres. According to the continuous-shape-measures (CShMs) method,⁶² the IrN_6 coordination spheres show a deviation parameter of 2.394 (**1**) and 2.570 (**2**) from the ideal O_h octahedral geometry, significantly higher than the deviation of 2.032 observed for the homoleptic $[\text{Ir}(\text{tpy})_2](\text{PF}_6)_3$ complex (Table S4, ESI†).

Photophysical properties

Absorption spectra

Room-temperature absorption spectra of complexes **1** and **2** measured in acetonitrile are shown in Fig. 2, and the photophysical data are reported in Table 1. For each complex, the spectrum displays intense absorption bands in the UV spectral window (200–330 nm), which are attributed to ligand centred (LC) $1\pi \rightarrow \pi^*$ transitions. The weaker bands tailing off above 330 nm are likely due to the charge transfer transition from Metal-to-Ligand (MLCT), with their nature being both spin allowed (singlet to singlet, $^1\text{MLCT}$) and spin forbidden (singlet-to-triplet, $^3\text{MLCT}$), as well as ligand-to-ligand and intra-ligand charge transfer transitions ($^3\text{LLCT}$ and $^3\text{ILCT}$). The spin forbidden transitions are enabled by the high spin–orbit coupling effect induced by the heavy Ir(III) metal centre.

Emission spectra

Fig. 3 shows the emission spectra of complexes **1**, **2** and the reference complex $[\text{Ir}(\text{tpy})_2](\text{PF}_6)_3$.⁶¹ For the latter, the highest energy band appears at $\lambda = 458$ nm, and its luminescence was

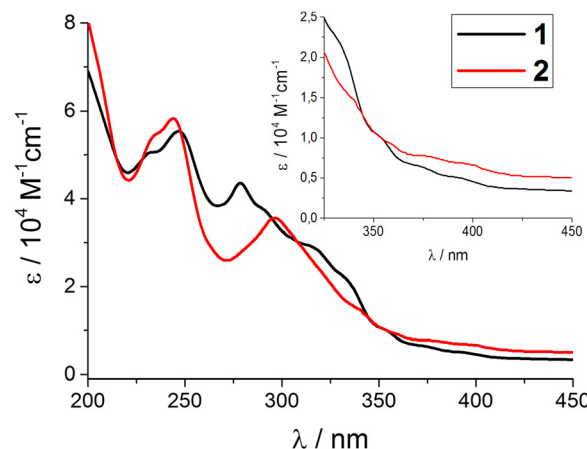


Fig. 2 Absorption spectra of complexes **1** (black) and **2** (red) (solvent: CH_3CN , $T = 298$ K).

ascribed mainly to ^3LC excited states with some minor contribution from $^3\text{MLCT}$ excited states.⁶¹ Complexes **1** and **2** exhibit green luminescence at room temperature in acetonitrile solutions. Both spectra are almost superimposable and display a vibrationally resolved profile quite similar to that shown by $[\text{Ir}(\text{tpy})_2](\text{PF}_6)_3$, although in these cases, the highest energy band maximum appears red shifted at $\lambda = 495$ nm. Their emissions show a monoexponential decay with lifetimes about 1.6 μs (**1**) and 1.2 μs (**2**), which increase to 5 μs and 3 μs , respectively, under an inert atmosphere. The emission quantum yields follow a similar trend, with values close to 1.5% in aerated solutions that rise by a factor of *ca.* 2.6 under oxygen-free conditions. For both complexes, the radiative (k_r) decay rate is close to $1 \times 10^4 \text{ s}^{-1}$, smaller than the $2.5 \times 10^4 \text{ s}^{-1}$ rate calculated for $[\text{Ir}(\text{tpy})_2](\text{PF}_6)_3$. These features indicate that the emission properties of both compounds arise from excited states with a prevalent ^3LC character, even if some $^3\text{MLCT}$ contribution cannot be ruled out.

Theoretical calculations

Time-dependent density functional theory (TD-DFT) was performed to gain further insight into the experimental absorption and emission properties described above. First, the molecular structures of complexes **1** and **2** were taken from the experimental X-ray crystal data and optimized by density functional theory (DFT) calculations using the CAM-B3LYP and B3LYP functionals with the 6-31G** + LANL2DZ basis sets and considering the solvent (acetonitrile) effects through the IEF-PCM formalism. From a structural point of view, the optimized geometries of the complexes in the ground state (S_0) fit well with those obtained from X-Ray data (Tables S2 and S3 in the ESI†). In particular, an excellent agreement between the experimental (RX) and computed bond distances involving the Ir(III) coordination sphere is found, with differences of just a few picometers in complexes **1** and **2**.

Second, the lowest singlet and triplet excited states were calculated at the optimized geometries of the ground states (S_0)



Table 1 Spectroscopic data for the compounds studied in this work

	1	2	1@SiO ₂	[Ir(tpy) ₂] ³⁺
Absorption				
$\lambda_{\text{max}}/\text{nm}$ ($10^{-4}\text{e}/\text{M}^{-1}\text{cm}^{-1}$)	230 (5.21), 244 (5.73), 276 (4.41), 287 (3.98), 310 (3.04), 328 (2.35), 348 (1.02), 369 (0.53), 390 (0.36)	232 (5.32), 241 (5.73), 294 (3.52), 337 (1.54), 373 (0.78), 398 (0.68)		210 (2.14), 221 (1.85), 251 (2.76), 277 (2.22), 313 (1.14), 325 (1.18), 336 (0.85), 352 (0.58), 374 (0.13)
Emission (CH₃CN solutions, $T = 298\text{ K}$)				
$\lambda_{\text{max}}/\text{nm}^a$	495, 531, 567(sh)	495, 532	498, 534, 570(sh)	458, 491, 523
$\tau_{\text{air}}/\mu\text{s}$	1.6	1.2	9.7 (99%), 40 (1%)	1.0
$\tau_{\text{dear}}/\mu\text{s}$	5	3	10.2 (98.5%), 42 (1.5%)	1.2
Φ_{air}	0.015	0.013	0.097	0.025
Φ_{dear}	0.042	0.033	0.093	—
$10^{-3}k_{\text{r}} (\text{s}^{-1})/10^{-5}k_{\text{nr}} (\text{s}^{-1})$	8.4/1.92	11.0/3.22	9.12/0.89	25/9.75 ^d
Emission (CH₃CN rigid matrix, $T = 77\text{ K}$)				
$\lambda_{\text{max}} (\text{nm})$	495, 532	495, 532	496, 534, 574	458
$\tau_{\text{air}}/\mu\text{s}$	13 (98%), 66 (2%)	26 (98%), 94 (2%)	16 (99%), 66 (1%)	26

^a $\lambda_{\text{exc}} = 375\text{ nm}$. ^b Radiative constant (deareated solutions): $k_{\text{r}} = \Phi/\tau$. ^c Non radiative constant: $k_{\text{nr}} = 1/\tau - k_{\text{r}}$. ^d k_{r} and k_{nr} calculated from τ_{air} and Φ_{air} values. ^e For the biexponential excited-state lifetimes, the relative weights of the exponential curves are indicated in parentheses.

using the TD-DFT approach and both CAM-B3LYP and B3LYP functionals. The computed T_1 geometries of both **1** and **2** are very similar to their respective S_0 geometries (Tables S2 and S3, ESI[†]). In addition, similar S_0 and T_1 geometries were obtained using CAM-B3LYP and B3LYP. The calculated CAM-B3LYP and B3LYP vertical electronic transitions and assignments of the complexes **1** and **2** are shown in Table 2 and Tables S5–S8 (ESI[†]). The frontier molecular orbitals involved in the dominant transitions are displayed in Fig. 4 and Fig. S8 (ESI[†]). The computed CAM-B3LYP wavelengths of the $S_0 \rightarrow S_1$ transitions for **1**: 319 nm and **2**: 321 nm are close to those observed in their experimental absorption spectra (Fig. 2 and Tables 1, 2), whereas those calculated with B3LYP are predicted to be red shifted at 380 nm and 382 nm for **1** and **2**, respectively (Tables S6 and S8, ESI[†]). We focus on the CAM-B3LYP assignments from now on for the sake of clarity (further details on the B3LYP results are shown in the ESI[†]). The $S_0 \rightarrow S_1$ optical transition for complex **2** is mainly assigned to the HOMO \rightarrow LUMO

Table 2 Calculated wavelengths and orbital transition analyses of the lowest energy absorption bands of complexes **1** and **2** at the CAM-B3LYP/6-31G** + LANL2DZ level of theory (only the electronic transitions involving the largest contribution percentages are listed)

Complex	Excited state	λ (nm)	E (eV)	f	Main assignments	MLCT (%)
1	$S_0 \rightarrow T_1$	471	2.63	0	HOMO \rightarrow LUMO+3 (27%) HOMO \rightarrow LUMO+1 (15%) HOMO-2 \rightarrow LUMO+1 (14%)	7.11
	$S_0 \rightarrow S_1$	319	3.89	0.0542	HOMO \rightarrow LUMO+1 (86%)	8.17
	$S_0 \rightarrow T_1$	473	2.62	0	HOMO \rightarrow LUMO+3 (21%) HOMO-1 \rightarrow LUMO+2 (19%) HOMO-2 \rightarrow LUMO (13%)	8.18
2	$S_0 \rightarrow S_1$	321	3.87	0.0458	HOMO \rightarrow LUMO (64%)	10.36

transition, whereas in the case of complex **1** it is assigned to HOMO \rightarrow LUMO+1 for symmetry reasons. Fig. 4 shows the energy and the atomic orbital composition calculated for the HOMO and LUMO of complexes **1** and **2**, together with those computed with CAM-B3LYP for the reference complex [Ir(tpy)₂](PF₆)₃ for comparison purposes. The HOMO of **1** is mainly localized on the Ir centre (11% of relative density distribution at the Ir atom) and the phenyltz ligand. In the case of the homoleptic complexes, *i.e.* the reference complex and complex **2**, the HOMO is localized in the two respective tpy and phenyltz ligands and the Ir centre (17% for **2**). However, the LUMO of **1** resides in its tpy ligand, occupying also only one of the two tpy ligands in the reference complex, whereas for **2** it is mainly located in the benzene and pyridine rings of its two phenyltz ligands. The LUMO+1 of **1**, which is close in energy to the LUMO (-2.02 eV), is located in its phenyltz ligand. Additionally, minor contributions from the central Ir(III) metal atoms to these LUMOs are found in **1** and **2** (3 and 2%, respectively). As a result, the $S_0 \rightarrow S_1$ absorptions can be mainly assigned to intraligand charge transfer (ILCT) for both compounds, together with a reduced MLCT character (8–10%).

If we compare the HOMO of the reference complex and that of **1**, the main effect of the additional tpy ligand in the reference

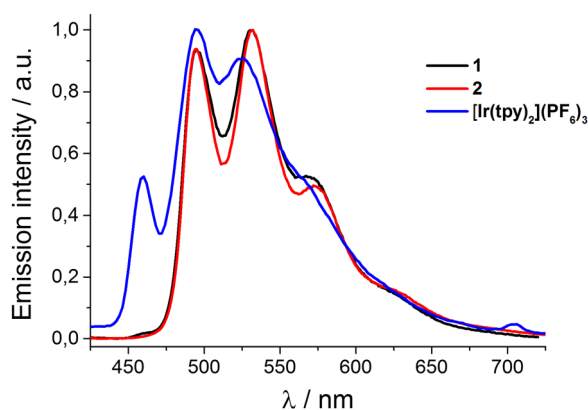


Fig. 3 Normalized emission spectra of complexes **1** (black) and **2** (red) in acetonitrile at 298 K. For comparative purposes, the emission spectrum of the reference complex [Ir(tpy)₂](PF₆)₃ measured in the same conditions is also displayed (blue).



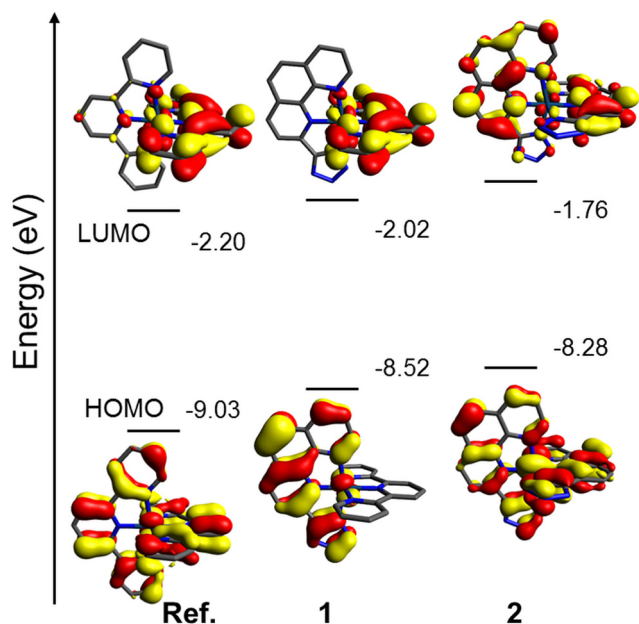


Fig. 4 Energy diagram showing the HOMO and LUMO frontier orbitals for the Ir(III) complexes **1** and **2** and the reference complex in acetonitrile solution at the CAM-B3LYP/6-31G** + LANL2DZ level of theory.

complex is the stabilization of its HOMO by 0.51 eV. The replacement of tpy (**1**) with phenttz (**2**) on going from **1** (−8.52 eV) to **2** (−8.28 eV) results in a destabilization of the HOMO by 0.24 eV. The LUMO of these complexes also follows the energy ordering of the reference complex (−2.20 eV) < **1** (−2.02 eV) < **2** (−1.76 eV), and presents identical molecular orbital topologies for **1** and the reference complex. Thus, theoretical calculations predict a higher HOMO–LUMO gap for the reference complex (−6.827 eV) with respect to **1** (−6.50 eV) and **2** (−6.52 eV), which is in agreement with the observation of a blue shift in the emission properties of the reference complex (Fig. 3), and the lack of observation of any shifts among the absorption and emission spectra of **1** and **2**.

Additionally, the phosphorescence wavelengths for $T_1 \rightarrow S_0$ after geometry optimization of the T_1 states of complexes **1** and **2** were computed using the vertical method and the CAM-B3LYP and B3LYP functionals with the 6-31G** + LANL2DZ basis sets (Table 3 and Table S9 and S10, ESI†). The former functional predicts the wavelengths for the $T_1 \rightarrow S_0$ emission transitions at 1017 nm and 486 nm for **1** and **2**, respectively. This method overestimates significantly the experimentally observed wavelength for $T_1 \rightarrow S_0$ in the case of **1**, which was associated to the stabilization of an artificial “ghost state”.⁶³ Actually, B3LYP predicts this $T_1 \rightarrow S_0$ transition at 664 nm for **1**,

which supports that statement, and at 482 nm for **2**, in good agreement with their experimental wavelengths (deviations in the range of 0.3–0.4 eV for **1** and **2**). Thus, the CAM-B3LYP computed absorption wavelengths for the lowest-energy transitions of **1** and **2** agreed better with the experimental absorption data than those obtained with B3LYP; whereas the latter functional reproduced better the experimental emission wavelengths. The $T_1 \rightarrow S_0$ emission of complexes **1** and **2** are assigned to HOMO \rightarrow LUMO transitions and incorporates $^3\text{ILCT}$ and a reduced $^3\text{MLCT}$ character (3–4%, Fig. S9 (ESI†) and Table 3). The HOMO and LUMO of the T_1 states of **1** and **2** are located on the phenttz ligand, that is, the only phenttz ligand in **1** and one of the two phenttz ligands in **2** (Fig. S9, ESI†).

Encapsulation of **1** in SiO_2 nanoparticles ($1@ \text{SiO}_2$)

We and others have demonstrated previously how the encapsulation of Ir(III) phosphors within amorphous silica nanoparticles serves to improve their photoluminescence properties. The silica matrix acts as a shelter protecting the complex from environmental quenchers such as oxygen and reduces its mobility, penalizing non-radiative deactivation pathways and leading to higher quantum efficiencies and longer emission lifetimes.^{48,64–67} Within this framework, we have prepared hybrid $1@ \text{SiO}_2$ following the reverse micelle protocol that we established previously to prepare $[\text{Ir}(\text{tpy})_2]@ \text{SiO}_2$.⁴⁸ First, PF_6^- counterions in **1** were replaced with NO_3^- by anion exchange chromatography in order to make the complex soluble in water. A water solution of this complex was added to a mixture of a surfactant in an organic solvent, leading to the formation of a water-in-oil microemulsion. Then, the hydrophilic silica precursor TEOS and a catalytic amount of ammonia were added, causing the hydrolysis and polymerization of TEOS inside the aqueous nuclei of the micelle containing the $[\text{Ir}(\text{tpy})_2]^{2+}$ complex. Thus, the cationic complex is embedded within the silica matrix and retained through strong electrostatic interactions with the negatively charged siloxyl groups of the silica. Following this procedure, we also tried to prepare the analogous sample $2@ \text{SiO}_2$, however, in this case a severe leakage of the $[\text{Ir}(\text{phenttz})_2]^+$ complex out of the silica matrix was evidenced during the synthetic washing and purification steps. This was probably due to the fact that the electrostatic interactions between the monocationic complex and the siloxyl groups were not strong enough to retain the complex in the silica matrix. In the case of $1@ \text{SiO}_2$, release of dicationic complex **1** in the washing solvents was negligible and allowed a full characterization of the sample.

Table 3 Calculated wavelengths and orbital transition analyses of the lowest energy emission bands of complexes **1** and **2** at the CAM-B3LYP/6-31G** + LANL2DZ level of theory. B3LYP computed wavelengths are also given. Only the electronic transitions involving the largest contribution percentages are listed

Complex	Excited state	λ (nm) CAM-B3LYP/B3LYP	E (eV) CAM-B3LYP/B3LYP	f	Main assignments	MLCT (%)
1	$T_1 \rightarrow S_0$	1017/664	1.22/1.87	0	HOMO \rightarrow LUMO (79%)	3.21
2	$T_1 \rightarrow S_0$	486/482	2.55/2.57	0	HOMO \rightarrow LUMO (79%)	4.01



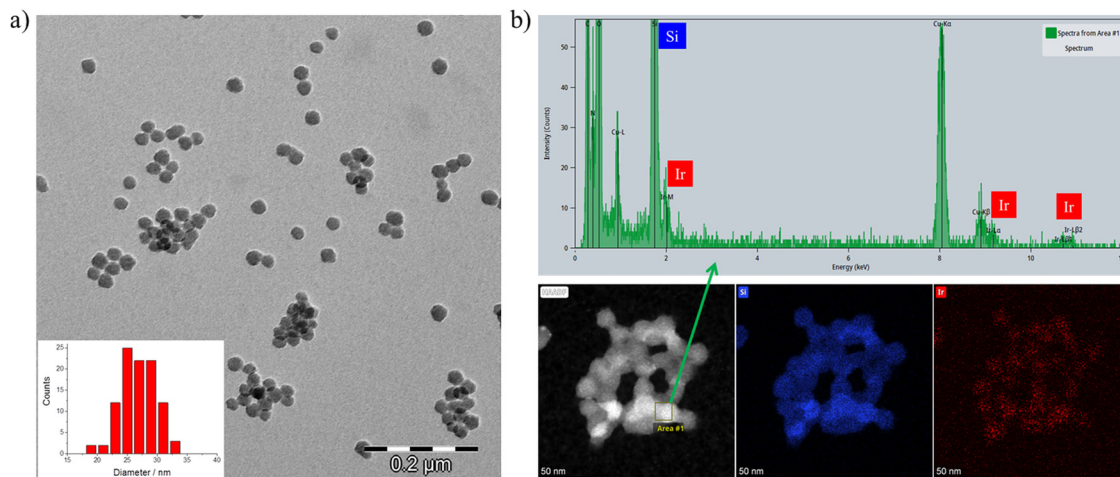


Fig. 5 (a) TEM image of **1@SiO₂** and size distribution histogram. (b) HAADF-STEM image and EDX compositional maps of **1@SiO₂**.

The morphology, size and composition of sample **1@SiO₂** were characterized by electron microscopy techniques. Fig. 5a and Fig. S8 (ESI[†]) show representative Transmission Electron Microscopy (TEM) images of the sample. The nanoparticles are spherical and monodisperse with an average size of 26.8 ± 2.9 nm. High-angle annular dark-field-scanning transmission electron microscopy (HAADF-STEM) and Energy Dispersive X-Ray (EDX) analysis confirm the encapsulation of the Ir(III) complex into the silica matrix.

Regarding the photophysical properties, the emission profiles of **1** and **1@SiO₂** are practically superimposable and no rigidochromic effect is observed, in accordance with a dominant ³LC character of the emissive excited state, which is not very sensitive to changes in the chemical environment around the Ir(III) complex. Conversely, significant differences in the emission intensity of both samples were observed. Compared to **1**, **1@SiO₂** is brighter and shows quantum yields and emission lifetimes that increase by factors of ~ 6.5 and ~ 2.2 in aerated and deaerated atmospheres, respectively. These facts indicate that the limited mobility of complex **1** in the rigid silica matrix restricts the vibrational motions and inhibits the non-radiative deactivation pathways of the excited state. This effect is clearly illustrated when the radiative (k_r) and non-radiative (k_{nr}) decay rates of **1** and **1@SiO₂** are compared (Table 1). $k_{r,rel}$ and $k_{nr,rel}$ are defined by eqn (1) and (2), respectively,

$$k_{r,rel} = \frac{k_{r,s}}{k_{r,f}} \quad (1)$$

$$k_{nr,rel} = \frac{k_{nr,s}}{k_{nr,f}} \quad (2)$$

where the subscripts *f* and *s* refer to free and silica encapsulated complex **1**, respectively. We observe that the radiative decay constants for **1** and **1@SiO₂** are almost identical ($k_{r,rel} = 1.09$), whereas the non-radiative rate of **1@SiO₂** decreases by a factor of *ca.* 2.15 compared to the free complex ($k_{nr,rel} = 0.46$). Finally, it is also important to highlight that silica prevents the quenching of the luminescence emission from environmental oxygen.

Whereas differences between the quantum yields and emission lifetimes for the free complex **1** in O₂/N₂ atmospheres are notable, these parameters remain almost identical for the encapsulated **1@SiO₂** sample.

Conclusions

In conclusion, two new cationic Ir(III) complexes derived from a tridentate tetrazole ligand, 2-(tetrazol-5-yl)-1,10-phenanthroline, have been prepared and fully characterized. Compared to the parent complex [Ir(ppy)₃]³⁺, a bathochromic shift of the emission is observed for **1** and **2**. TD-DFT calculations reveal that in both cases the emission is centred in the phenanthroline-tetrazolate moiety and exhibits a prominent ³ILCT character and a minor ³MLCT. Both complexes are robust enough to be embedded into silica nanoparticles, although only the dicationic complex **1** remains inside the nanoparticles when in contact with water. This is due to strong electrostatic interactions with the negatively charged silanol groups of the nanoparticles. The rigid silica matrix serves to improve the emission yield and extend the emission lifetime of **1**, as the mobility of the complex is restricted. Considering the wide variety of tridentate tetrazole-based ligands already described in the literature, a vast family of homo- and/or heteroleptic Ir(III) complexes with color emissions ranging in the whole visible spectral window can be prepared. These Ir(III) compounds could be used as neutral emitters for OLEDs, cationic luminophores for LEEC devices or biocompatible silica-based biomarkers. Some of these possibilities are currently under investigation in our laboratory.

Author contributions

J. M. H. supervised the project and provided financial support. J. T. synthesized the complexes and performed the chemical characterization. J. M. H. carried out the structural characterization. M. M. Q. M. performed the DFT and TD-DFT calculations. J. R. J. performed the photophysical characterization.



J. M. H. and M. M. Q. M. wrote the manuscript and all the authors approved its final version.

Conflicts of interest

The authors declare no competing financial interest.

Acknowledgements

This research was financially supported by MCIN/AEI/10.13039/201100011033/FEDER “Una manera de hacer Europa (Project PGC2018-102052-B-C21); The Junta de Andalucía (FQM-195), FEDER/Junta de Andalucía-Consejería de Transformación Económica, Industria, Conocimiento y Universidades, Projects A-FQM-172-UGR18 and B.FQM.328.UGR20 and the University of Granada. The authors acknowledge the technical support provided by the Centro de Instrumentación Científica (CIC) of the University of Granada, the technician César López-Ruiz, and the Centro de Servicios de Informática y Redes de Comunicaciones (CSIRC) for computational time and facilities. M. M. Q. M. thanks Junta de Andalucía for a postdoctoral fellowship (DOC_01282). M. M. Q. M. and J. R. J. also thank Ministerio de Ciencia, Innovación y Universidades for Juan de la Cierva formación and incorporación contracts (grants FJC2018-035709-I and IJC2020-044040-I supported by MCIN/AEI/10.13039/501100011033). We also acknowledge Amparo Navarro and Tomás Peña Ruiz for insightful discussions and help with the quantum-chemical calculations.

References

- 1 A. Verma, B. Kaur, S. Venugopal, P. Wadhwa, S. Sahu, P. Kaur, D. Kumar and A. Sharma, *Chem. Biol. Drug Des.*, 2022, **100**, 419–442.
- 2 C. Gao, L. Chang, Z. Xu, X. F. Yan, C. Ding, F. Zhao, X. Wu and L. S. Feng, *Eur. J. Med. Chem.*, 2019, **163**, 404–412.
- 3 A. J. Mota, a Rodríguez-Diéguez, M. a Palacios, J. M. Herrera, D. Luneau and E. Colacio, *Inorg. Chem.*, 2010, **49**, 8986–8996.
- 4 S. Vorona, T. Artamonova, Y. Zevatskii and L. Myznikov, *Synthesis*, 2014, 781–786.
- 5 J. Roh, K. Vávrová and A. Hrabálek, *Eur. J. Org. Chem.*, 2010, 6101–6118.
- 6 Z. P. Demko and K. B. Sharpless, *J. Org. Chem.*, 2001, **66**, 7945–7950.
- 7 M. Dincă, W. S. Han, Y. Liu, A. Dailly, C. M. Brown and J. R. Long, *Angew. Chem., Int. Ed.*, 2007, **46**, 1419–1422.
- 8 A. Rodríguez, R. Kivekäs and E. Colacio, *Chem. Commun.*, 2005, 5228–5230.
- 9 X. He, C.-Z. Lu and D.-Q. Yuan, *Inorg. Chem.*, 2006, **45**, 5760–5766.
- 10 A. Rodríguez-Diéguez and E. Colacio, *Chem. Commun.*, 2006, 4140–4142.
- 11 R.-G. Xiong, X. Xue, H. Zhao, X.-Z. You, B. F. Abrahams and Z. Xue, *Angew. Chem., Int. Ed.*, 2002, **41**, 3800–3803.
- 12 X. Xue, X.-S. Wang, L.-Z. Wang, R.-G. Xiong, B. F. Abrahams, X.-Z. You, Z.-L. Xue and C.-M. Che, *Inorg. Chem.*, 2002, **41**, 6544–6546.
- 13 A. J. Mota, a Rodríguez-Diéguez, M. a Palacios, J. M. Herrera, D. Luneau and E. Colacio, *Inorg. Chem.*, 2010, **49**, 8986–8996.
- 14 W. Zhang, F. Zhao, T. Liu, M. Yuan, Z.-M. Wang and S. Gao, *Inorg. Chem.*, 2007, **46**, 2541–2555.
- 15 M. Giraud, E. S. Andreiadis, A. S. Fisyuk, R. Demadrille, J. Pécaut, D. Imbert and M. Mazzanti, *Inorg. Chem.*, 2008, **47**, 3952–3954.
- 16 E. S. Andreiadis, R. Demadrille, D. Imbert, J. Pécaut and M. Mazzanti, *Chemistry*, 2009, **15**, 9458–9476.
- 17 N. M. Shavaleev, S. V. Eliseeva, R. Scopelliti and J.-C. G. Bünzli, *Inorg. Chem.*, 2014, **53**, 5171–5178.
- 18 E. S. Andreiadis, D. Imbert, J. Pécaut, R. Demadrille and M. Mazzanti, *Dalton Trans.*, 2012, **41**, 1268–1277.
- 19 G. Bozoklu, C. Marchal, J. Pécaut, D. Imbert and M. Mazzanti, *Dalton Trans.*, 2010, **39**, 9112–9122.
- 20 C. A. Tovee, C. A. Kilner, J. A. Thomas and M. A. Halcrow, *CrystEngComm*, 2009, **11**, 2032.
- 21 S. Di Pietro, D. Imbert and M. Mazzanti, *Chem. Commun.*, 2014, **50**, 10323–10326.
- 22 J. R. Jiménez, I. F. Díaz-Ortega, E. Ruiz, D. Aravena, S. J. A. Pope, E. Colacio and J. M. Herrera, *Chem. – Eur. J.*, 2016, **22**, 14548–14559.
- 23 M. Duati, S. Tasca, F. C. Lynch, H. Bohlen, J. G. Vos, S. Stagni and M. D. Ward, *Inorg. Chem.*, 2003, **42**, 8377–8384.
- 24 S. Stagni, E. Orselli, A. Palazzi, L. De Cola, S. Zacchini, C. Femoni, M. Marcaccio, F. Paolucci and S. Zannarini, *Inorg. Chem.*, 2007, **46**, 9126–9138.
- 25 D. S. Silvester, S. Uprety, P. J. Wright, M. Massi, S. Stagni and S. Muzzioli, *J. Phys. Chem. C*, 2012, **116**, 7327–7333.
- 26 P. J. Wright, S. Muzzioli, M. V. Werrett, P. Raiteri, B. W. Skelton, D. S. Silvester, S. Stagni and M. Massi, *Organometallics*, 2012, **31**, 7566–7578.
- 27 M. V. Werrett, D. Chartrand, J. D. Gale, G. S. Hanan, J. G. MacLellan, M. Massi, S. Muzzioli, P. Raiteri, B. W. Skelton, M. Silberstein and S. Stagni, *Inorg. Chem.*, 2011, **50**, 1229–1241.
- 28 C. A. Strassert, C.-H. Chien, M. D. Galvez Lopez, D. Kourkoulos, D. Hertel, K. Meerholz and L. De Cola, *Angew. Chem., Int. Ed.*, 2011, **50**, 946–950.
- 29 N. K. Allampally, C. A. Strassert and L. De Cola, *Dalton Trans.*, 2012, **41**, 13132.
- 30 C. Cebrián, M. Mauro, D. Kourkoulos, P. Mercandelli, D. Hertel, K. Meerholz, C. A. Strassert and L. De Cola, *Adv. Mater.*, 2013, **25**, 437–442.
- 31 K. D. M. MaGee, P. J. Wright, S. Muzzioli, C. M. Siedlowskas, P. Raiteri, M. V. Baker, D. H. Brown, S. Stagni and M. Massi, *Dalton Trans.*, 2013, **42**, 4233.
- 32 P. Brulatti, V. Fattori, S. Muzzioli, S. Stagni, P. P. Mazzeo, D. Braga, L. Maini, S. Milita and M. Cocchi, *J. Mater. Chem. C*, 2013, **1**, 1823.
- 33 N. K. Allampally, M. Bredol, C. A. Strassert and L. De Cola, *Chem. – A Eur. J.*, 2014, **20**, 16863–16868.



- 34 J. Sanning, L. Stegemann, M. Nyenhuis, C. G. Daniliuc, N. L. Doltsinis and C. A. Strassert, *Z. Naturforsch., B: J. Chem. Sci.*, 2016, **71**, 463–473.
- 35 M. E. Robinson, A. Nazemi, D. J. Lunn, D. W. Hayward, C. E. Boott, M.-S. Hsiao, R. L. Harniman, S. A. Davis, G. R. Whittell, R. M. Richardson, L. De Cola and I. Manners, *ACS Nano*, 2017, **11**, 9162–9175.
- 36 H. Geng, K. Luo, G. Zou, L. Zhao, H. Wang, Q. Li and H. Ni, *Dyes Pigm.*, 2018, **149**, 82–91.
- 37 L.-L. Wu, C.-H. Yang, I.-W. Sun, S.-Y. Chu, P.-C. Kao and H.-H. Huang, *Organometallics*, 2007, **26**, 2017–2023.
- 38 S.-J. Yeh, M.-F. Wu, C.-T. Chen, Y.-H. Song, Y. Chi, M.-H. Ho, S.-F. Hsu and C. H. Chen, *Adv. Mater.*, 2005, **17**, 285–289.
- 39 S. Stagni, S. Colella, A. Palazzi, G. Valenti, S. Zacchini, F. Paolucci, M. Marcaccio, R. Q. Albuquerque and L. De Cola, *Inorg. Chem.*, 2008, **47**, 10509–10521.
- 40 F. Monti, A. Baschieri, I. Gualandi, J. J. Serrano-Pérez, J. M. Junquera-Hernández, D. Tonelli, A. Mazzanti, S. Muzzioli, S. Stagni, C. Roldan-Carmona, A. Pertegás, H. J. Bolink, E. Ortí, L. Sambri and N. Armaroli, *Inorg. Chem.*, 2014, **53**, 7709–7721.
- 41 V. Fiorini, A. D'Ignazio, K. D. M. Magee, M. I. Ogden, M. Massi and S. Stagni, *Dalton Trans.*, 2016, **45**, 3256–3259.
- 42 V. Fiorini, N. Monti, G. Vigarani, G. Santi, F. Fasulo, M. Massi, L. Giorgini, A. B. Muñoz-García, M. Pavone, A. Pucci and S. Stagni, *Dyes Pigm.*, 2021, **193**, 109532.
- 43 Y. Chi, T. K. Chang, P. Ganesan and P. Rajakannu, *Coord. Chem. Rev.*, 2017, **346**, 91–100.
- 44 B. Tong, H. Y. Ku, I. J. Chen, Y. Chi, H. C. Kao, C. C. Yeh, C. H. Chang, S. H. Liu, G. H. Lee and P. T. Chou, *J. Mater. Chem. C*, 2015, **3**, 3460–3471.
- 45 C.-W. Lu, Y. Wang and Y. Chi, *Chem. – A Eur. J.*, 2016, **22**, 17892–17908.
- 46 J. Lin, Y. Wang, P. Gnanasekaran, Y.-C. Chiang, C.-C. Yang, C.-H. Chang, S.-H. Liu, G.-H. Lee, P.-T. Chou, Y. Chi and S.-W. Liu, *Adv. Funct. Mater.*, 2017, **27**, 1702856.
- 47 L.-Y. Hsu, D.-G. Chen, S.-H. Liu, T.-Y. Chiu, C.-H. Chang, A. K.-Y. Jen, P.-T. Chou and Y. Chi, *ACS Appl. Mater. Interfaces*, 2020, **12**, 1084–1093.
- 48 S. Titos-Padilla, E. Colacio, S. J. A. Pope, J. J. Delgado, M. Melgosa and J. M. Herrera, *J. Mater. Chem. C*, 2013, **1**, 3808–3815.
- 49 G. M. Sheldrick, *Acta Crystallogr., Sect. A: Found. Crystallogr.*, 2008, **64**, 112–122.
- 50 O. V. Dolomanov, L. J. Bourhis, R. J. Gildea, J. A. K. Howard and H. Puschmann, *J. Appl. Crystallogr.*, 2009, **42**, 339–341.
- 51 T. Yanai, D. P. Tew and N. C. Handy, *Chem. Phys. Lett.*, 2004, **393**, 51–57.
- 52 A. D. Becke, *J. Chem. Phys.*, 1993, **98**, 5648–5652.
- 53 A. D. Becke, *Phys. Rev. A: At., Mol., Opt. Phys.*, 1988, **38**, 3098–3100.
- 54 C. Lee, W. Yang and R. G. Parr, *Phys. Rev. B: Condens. Matter Mater. Phys.*, 1988, **37**, 785–789.
- 55 Y. Yang, M. N. Weaver and K. M. Merz, *J. Phys. Chem. A*, 2009, **113**, 9843–9851.
- 56 C. Latouche, D. Skouteris, F. Palazzetti and V. Barone, *J. Chem. Theory Comput.*, 2015, **11**, 3281–3289.
- 57 S. N. Genin, I. G. Ryabinkin, N. R. Paisley, S. O. Whelan, M. G. Helander and Z. M. Hudson, *Angew. Chem., Int. Ed.*, 2022, **61**, e202116175.
- 58 J. Tomasi, B. Mennucci and R. Cammi, *Chem. Rev.*, 2005, **105**, 2999–3094.
- 59 M. J. Frisch, G. W. Trucks, H. B. Schlegel, G. E. Scuseria, M. A. Robb, J. R. Cheeseman, G. Scalmani, V. Barone, B. Mennucci, G. A. Petersson, H. Nakatsuji, M. Caricato, X. Li, H. P. Hratchian, A. F. Izmaylov, J. Bloino, G. Zheng, J. L. Sonnenberg, M. Hada, M. Ehara, K. Toyota, R. Fukuda, J. Hasegawa, M. Ishida, T. Nakajima, Y. Honda, O. Kitao, H. Nakai, T. Vreven, J. A. Montgomery Jr., J. E. Peralta, F. Ogliaro, M. Bearpark, J. J. Heyd, E. Brothers, K. N. Kudin, V. N. Staroverov, R. Kobayashi, J. Normand, K. Raghavachari, A. Rendell, J. C. Burant, S. S. Iyengar, J. Tomasi, M. Cossi, N. Rega, J. M. Millam, M. Klene, J. E. Knox, J. B. Cross, V. Bakken, C. Adamo, J. Jaramillo, R. Gomperts, R. E. Stratmann, O. Yazyev, A. J. Austin, R. Cammi, C. Pomelli, J. W. Ochterski, R. L. Martin, K. Morokuma, V. G. Zakrzewski, G. A. Voth, P. Salvador, J. J. Dannenberg, S. Dapprich, A. D. Daniels, Ö. Farkas, J. B. Foresman, J. V. Ortiz, J. Cioslowski and D. J. Fox, *Gaussian 09, Revision B.01*, Gaussian, Inc., Wallingford, CT, 2010.
- 60 M. D. Hanwell, D. E. Curtis, D. C. Lonie, T. Vandermeersch, E. Zurek and G. R. Hutchison, *J. Cheminf.*, 2012, **4**, 17.
- 61 J. P. Collin, I. M. Dixon, J. P. Sauvage, J. A. G. Williams, F. Barigelletti and L. Flamigni, *J. Am. Chem. Soc.*, 1999, **121**, 5009–5016.
- 62 S. Alvarez, P. Alemany, D. Casanova, J. Cirera, M. Llunell and D. Avnir, *Coord. Chem. Rev.*, 2005, **249**, 1693–1708.
- 63 L. Goerigk and S. Grimme, *J. Chem. Phys.*, 2010, **132**, 184103.
- 64 I. Zanoni, V. Fiorini, M. Rosado, B. Ballesteros, M. Androulidaki, M. Blosi, S. Ortelli, S. Stagni, M. Dondi and A. L. Costa, *New J. Chem.*, 2018, **42**, 9635–9644.
- 65 C.-W. Lai, Y.-H. Wang, C.-H. Lai, M.-J. Yang, C.-Y. Chen, P.-T. Chou, C.-S. Chan, Y. Chi, Y.-C. Chen and J.-K. Hsiao, *Small*, 2008, **4**, 218–224.
- 66 S. Zanarini, E. Rampazzo, S. Bonacchi, R. Juris, M. Marcaccio, M. Montalti, F. Paolucci and L. Prodi, *J. Am. Chem. Soc.*, 2009, **131**, 14208–14209.
- 67 O.-H. Kim, S.-W. Ha, J. Il Kim and J.-K. Lee, *ACS Nano*, 2010, **4**, 3397–3405.

